RSC Advances

ROYAL SOCIETY OF CHEMISTRY

www.rsc.org/advances

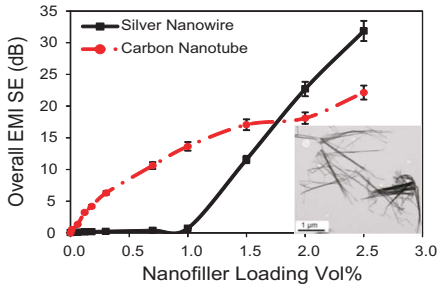

Synthesized silver nanowire/polystyrene nanocomposites showed superior electrical properties to commercial carbon nanotube/polystyrene nanocomposites at high filler loadings. This was ascribed to higher metallic nature of silver nanowires.

Outstanding Electromagnetic Interference Shielding of Silver Nanowire: Comparison with Carbon Nanotube

Mohammad Arjmand, Aref Abbasi Moud, Yan Li,

Uttandaraman Sundararaj*

Department of Chemical and Petroleum Engineering, University of Calgary, Calgary, Canada

*Corresponding author. Tel/Fax: +1 403 2106549/+1 403 2844852.
E-mail address: u.sundararaj@ucalgary.ca (U. Sundararaj)
E-mail address: marjmand@ucalgary.ca (M. Arjmand)

Abstract

Silver nanowires (AgNWs) were synthesized by AC electrodeposition of Ag into porous aluminum oxide templates. AgNWs were embedded into polystyrene via a solution processing technique to create a nanocomposite. For comparison, carbon nanotube (CNT)/polystyrene nanocomposites were generated identically. TEM and XRD analyses confirmed the synthesis of AgNWs with average diameter and length of 25nm and 3.2μm, respectively. TEM images also revealed that at molding temperature (240ºC) AgNWs transformed into a chain of nanospheres. At low filler loadings, the AgNW/polystyrene nanocomposites presented inferior electrical properties compared to CNT/polystyrene nanocomposites. This was attributed to lower aspect ratio, fragmentation phenomenon and poorer conductive network for AgNWs. However, at high filler loadings, the electrical properties of the AgNW/polystyrene nanocomposites significantly surpassed. It seems that at high filler loadings, the conductive network was well-established for both types of nanocomposites and thus, higher innate conductivity of AgNWs played a dominant role in presenting superior electrical properties.

Keywords: Carbon Nanotube; Silver Nanowire; Electrical Conductivity; Electromagnetic Interference Shielding; Dielectric Properties; Electron Microscopy; X-ray Diffraction

1. Introduction

The increase in using electronic devices for telecommunication and computation has heightened the need to resolve the issue of electromagnetic interference (EMI). Emitted electromagnetic (EM) waves from electronics bring up a serious concern in society as they are potentially hazardous for the health of human body and efficacy of devices [1, 2].

The performance of shields to attenuate EM waves is assessed by shielding effectiveness (*SE*). The *SE* of a material is defined as the logarithm of the ratio of incident power to transmitted power and its unit is expressed in dB:

$$SE = 10 \log\left(\frac{P_i}{P_0}\right) \quad (1)$$

where P_i is the incident power and P_0 is the transmitted power. Time-averaged power is proportional to the root mean square (rms) of the electric field strength; therefore Equation 1 can also be rewritten as:

$$SE = 20 \log\left(\frac{E_i}{E_0}\right) \quad (2)$$

where E_i and E_0 are the incident and transmitted electric field strengths, respectively [3]. Commercially, 99.9% attenuation of incident EM waves, corresponding to *SE* of 30dB, is considered sufficient for many practical engineering applications [4-6].

In order to minimize the undesirable effects of EM waves, several novel materials have been developed [7, 8], among which, metal coated polymers, ICPs (intrinsically conductive polymers) and conductive filler/polymer composites (CPCs) are the most common. Metal

coated polymers exhibit drawbacks such as delamination of metal, poor adhesion between layers and environmental hazards. The commercialization of ICPs is also very limited due to poor long-term stability and lack of industrial processing methods. The aforementioned problems give CPCs an edge for use as futuristic shielding materials. CPCs benefit from inherent properties of polymers, such as light weight, low cost, easy processability and corrosion resistance, coupled with adjustable electrical properties originating from controlling the level of conductive network formation [9].

Designing a CPC with a high EMI shielding capability should be performed by considering processing and economic parameters. Overloading fillers well over percolation threshold makes nanocomposites expensive and heavy, while underloading makes the system and its environment vulnerable to EM waves. EMI shielding capability of a CPC relies on two main factors: (1) intrinsic properties of filler, such as filler's innate electrical conductivity, diameter and aspect ratio [10, 11], and (2) processing-related factors such as dispersion, distribution and orientation of fillers [12].

It has been proved both theoretically and experimentally that conductive shields comprising fillers with higher aspect ratio (higher length and/or lower diameter) provide lower percolation threshold, and higher electrical conductivity and EMI shielding [13-17]. It is well known that the surface area of a unit mass of a filler has an inverse relationship with its diameter, and fillers with higher length have more probability to come close to or contact each other. For example, Al-Saleh and Sundararaj [18] compared the EMI shielding of high structure nano-sized carbon black and multi-walled carbon nanotube (MWCNT) in the X-band frequency range, and showed that at 7.5vol%, the EMI shielding of MWCNT was

almost double of carbon black (35dB versus 18dB). In another study, Huang et al. [17] studied the effect of aspect ratio on percolation threshold and EMI shielding by comparing long and short MWCNTs. Their result showed longer MWCNTs offered lower percolation threshold and higher shielding.

The impacts of processing parameters on the electrical properties of CPCs were also well reviewed in the literature [19-22]. Arjmand et al. [23] observed a huge effect of orientation of MWCNTs on the conductivity and EMI shielding. It was shown that orientation affects the level of conductive network formation, and therefore changes the attenuation ability of CPCs. Im et al. [12] studied carbon black/polyaniline system, and enhanced the affinity of carbon black toward polyaniline by fluorination. Their results showed that enhanced adhesion between the host matrix and filler led to a better dispersion and therefore higher conductivity and EMI shielding.

For efficient shielding, shields must possess mobile charge carriers and/or electric/magnetic dipoles to interact with electric/magnetic vectors of an incident EM wave [24, 25]. This amplifies the importance of the inherent properties of fillers embedded in CPCs. Regarding the choice of fillers, MWCNTs are proposed as promising candidates due to their huge surface area, high electrical conductivity, significant corrosion resistance and industrial growth. Moreover, MWCNTs have long mean-free-paths and extremely high current densities, which both are vital to shielding. These properties commend MWCNTs as excellent fillers for EMI shielding applications [26].

Despite the fascinating properties of MWCNTs, their lower electrical conductivity limits their use in advanced applications. Accordingly, metallic nanowires, as a new class of nanofillers, with superior electrical conductivity have been introduced to fill the aforementioned gap. Copper is the main metallic nanowire used for EMI shielding; however, it is readily oxidized under atmospheric conditions [27]. This brings up the idea of using silver (Ag) nanowires as they have higher electrical conductivity than copper ($6.30\times10^{+5}$ S·cm^{-1} versus $5.96\times10^{+5}$ S·cm^{-1}) along with greater resistance to oxidation [28, 29]. Accordingly, the literature comprises several studies that employed AgNWs as conductive nanofillers in CPCs with the focus on electrical conductivity [30-33], or EMI shielding behavior [34-36].

Yu et al. [35] synthesized AgNWs with polyol technique and then mixed them with epoxy matrix using an ex-situ process. According to their results, AgNW/epoxy composites presented lower percolation threshold and superior EMI shielding compared to their Ag nanoparticles counterparts. They ascribed this discrepancy to higher aspect ratio of nanowires relative to nanoparticles. In another study, Ma et al. [34] made ultralightweight AgNW/polyimide composite foams with microcellular structure and reported an EMI SE of 1210 dB·g^{-1}·cm^3 at 200MHz.

All the mentioned studies employed polyol technique to synthesize AgNW with the diameter ranging ~ 100-200nm. Nonetheless, in the current study we synthesized AgNW by AC electrodeposition of Ag into porous aluminum oxide template, and were able to generate AgNWs with significantly lower diameter. Low diameter of conductive nanofiller is highly important for EMI shielding applications. We also interestingly observed the

fragmentation phenomenon of AgNW during the melt mixing process, which was not reported in previous studies. Moreover, in order to evaluate the merit of AgNWs for shielding applications, we compared the electrical properties of AgNW/polymer nanocomposites with MWCNT/polymer nanocomposites, i.e. electrical conductivity, EMI shielding, imaginary permittivity and real permittivity. Correlating the percolation curves with the EMI shielding of the generated nanocomposites implied a tight correlation between EMI shielding performance and level of conductive network formation.

2. Experimental

2.1. Materials and nanocomposites preparation

2.1.1. Synthesis of AgNWs

The most widely used method for generating metallic nanowires with less than 50nm diameter is still template-directed synthesis, which involves either chemical or electrochemical deposition [29]. Aluminum plates (5cm × 11cm) with 1mm thickness were used as primary templates. The aluminum plates were anodized in parallel by immersing in a large tank filled with 0.3M H_2SO_4 at 2°C. Counter-electrodes were stainless steel plates with the same dimensions as the aluminum plates. The growth of the porous aluminum oxide (alumina) templates was performed in two steps: in the first step, the plates were immersed in a 0.3M H_2SO_4 solution for 2hr under 25.0V to create initial porous structure. Afterwards, the plates were placed in a 1:1 mixture of 0.2M H_2CrO_4 and 0.6M H_3PO_4 at 60°C for 30min to make the already formed porous structure more uniform. In the next

step, the plates were reimmersed in the 0.3M H_2SO_4 solution for 8hr, and then the applied voltage was reduced incrementally to reduce the alumina barrier layer at the pore bottom. Thinning the alumina barrier is a crucial part of the process since it keeps the end of the porous structure electrically conductive for the electrodeposition process. The protocol to decrease the voltage was initiated by a reduction rate of 2V/min from 25V to 15V; then it was followed by a 1V/min rate to 9V, and eventually after 5min keeping at 9V, the voltage was dropped to zero. These synthesis steps generated cylindrical pores with hexagonal cross sections [37].

AC electrodeposition of Ag into the hexagonal-shaped pores was accomplished by insulating the edges of the electrodes by applying nail polish, and then immersing the plates for 5min in an electrolyte solution of silver sulfate (Ag_2SO_4, 8.5g/L), diammonium hydrogen citrate ($(NH_4)_2HC_6H_5O_7$, 200g/L), and potassium thiocyanate (KSCN, 105g/L). Square wave voltage pulses were applied between the Al plates and two pure Ag counter-electrodes to push the Ag ions toward the end of the pores. The voltage pulses were applied at 100Hz frequency and ±8.0V peaks (pulsed every 400ms) for 1.5hr.

Liberation of the nanowires was started by physical removing of the bulk-deposited Ag from the surface of the Al plates, and then AgNWs were liberated from porous alumina in a beaker filled with 1.0M NaOH(aq) at room temperature. NaOH(aq) dissolved the surrounding alumina sheath so that we could recover the individual nanowires. After the liberation, floating fragments (bundled nanowires) were collected into a 1:1 mixture of 0.1M NaOH(aq) and MeOH, and sonicated for 10min. Immediately afterwards, collected AgNWs were purified through filter paper (Whatman with less than 1μm pore size), rinsed

with MeOH, and then transferred to a beaker containing 100mL of MeOH. Additional details on the synthesis of the AgNWs can be found elsewhere [38].

2.1.2. AgNW and MWCNT nanocomposites preparation

Nanocomposites were prepared by the miscible solvent mixing and precipitation (MSMP) technique [37]. The nanocomposites with different concentrations of AgNWs were produced by mixing different volumes of 3.3mg/ml AgNW/MeOH suspension with 20mg/ml polystyrene (PS) (Styron® 615 APR, Americas Styrenics LLC)/methylene chloride solution. Each mixture was treated in an ultrasound bath for 30min, and then stirred for 10min prior to mixing. The suspension was then filtered and placed in an evaporation dish for 16h in a fume hood. The residue was further dried in a vacuum oven at 50°C for 24hr to obtain nanocomposite nuggets. The polymer nanocomposite nuggets were then molded into a rectangular cavity, with the dimensions of 10.16×22.86×0.87mm, at 240°C and 38MPa for 15min. For the sake of comparison, MWCNT/PS nanocomposites were produced at the same volumetric concentrations with the same technique. MWCNTs (Nanocyl™ NC7000) were obtained from Nanocyl S.A. (Sambreville, Belgium).

2.2. Materials characterization

The TEM analyses of the nanofillers and nanocomposites were carried out on a Tecnai TF20 G2 FEG-TEM (FEI, Hillsboro, Oregon, USA) at 200kV acceleration voltage with a

standard single-tilt holder. The images were taken with a Gatan UltraScan 4000 CCD (Gatan, Pleasanton, California, USA) at 2048×2048 pixels. For the TEM analyses of the nanofillers, the droplets of AgNW and MWCNT suspensions were placed on a holey carbon-coated Cu TEM grid, and dried at room condition. For the TEM analyses of the nanocomposites, the molded nanocomposites were ultramicrotomed to achieve 70nm thick sections.

Both molded nanocomposites and powdery liberated AgNWs were analyzed with X-ray diffraction (XRD). The XRD analysis was performed using a Rigaku ULTIMA III X-ray diffractometer with Cu K-alpha radiation as the X-ray source. The scan was carried out in the range 2θ=30–90 degrees using a 0.02 degree step and a counting time of 1 degree per minute at 40kV and 44mA to obtain the full diffractogram for the materials.

The electrical conductivity measurements were carried out on the molded rectangular samples. All the samples' surfaces were wiped with ethanol to remove impurities prior to the measurements. For nanocomposites with electrical conductivities more than $10^{-4}S\cdot cm^{-1}$, we carried out the measurements according to ASTM 257-75 using a Loresta GP resistivity meter (MCPT610 model, Mitsubishi Chemical Co., Japan). A standard four-pin probe was used to reduce the effect of contact resistance. For an electrical conductivity less than $10^{-4}S\cdot cm^{-1}$, a Keithley 6517A electrometer connected to a Keithley 8009 test fixture (Keithley Instruments, USA) was used.

The EMI shielding measurements were carried out over the X-band (8.2–12.4GHz) frequency range using an E5071C network analyzer (ENA series 300KHz – 20GHz). The

samples under the test were squeezed between two flanges connecting the waveguides of the network analyzer. The network analyzer sent a signal down the waveguide incident to the sample, and then the scattering parameters (S-parameters) of each sample were recorded, and used to calculate *SE*. The dielectric properties of the generated nanocomposites were also obtained via conversion of the measurements using Reflection/Transmission Mu and Epsilon Nicolson-Ross Model.

3. Results and Discussion

3.1. Morphology

In order to obtain essential information about the morphology of AgNWs, the TEM images of AgNWs were captured before and after the processing. Figure 1(a) displays the bundles of pristine AgNWs with uniform length before processing, demonstrating the ability of the synthesis method to produce AgNWs with uniform dimensions. The statistical analysis of over 100 AgNWs indicated that AgNWs had an average diameter, length and aspect ratio of 25nm, 3.2μm and 128, respectively. The synthesized AgNWs showed much lower diameter, and consequently higher surface area, compared to AgNWs synthesized by Ma et al. [34] (90nm), Yu et al. [35] (100-200nm), and Sureshkumar et al. [33] (112nm).

As depicted in Figure 1(b), despite the long sonication time, some portions of AgNWs are still bundled in the PS matrix. This can be ascribed to large surface area and huge van der Waals forces between AgNWs, and this agglomeration can adversely affect the electrical properties. Gelves et al. [38] also showed the irreversible agglomeration of clean

nanowires after liberation. Figure 1(c) shows that MWCNTs were relatively well dispersed and distributed in the PS matrix, promising enhanced electrical properties.

TEM images of AgNWs after the processing revealed that during the mixing process, AgNWs became unstable and surprisingly lost their original shape and aspect ratio and broke into short cylinders with bulbous ends or into spheres (Figure 1(b)). Deformation of AgNWs during the mixing process at high temperature can be ascribed to fragmentation phenomenon, which has been reported in the literature [39]. This observation is quite significant due to the significant impact of the filler's aspect ratio on the final electrical properties of CPCs.

The fragmentation phenomenon is believed to change the shape of nanowires from a cylinder to a linear row of nanospheres at high temperatures, where atomic movements by diffusion become fairly important [40-44]. Karim et al. [41] observed the fragmentation for gold nanowires at 600°C, and believed that the fragmentation arises from thickness undulation along the axis of the nanowires followed by spheroidization. In another study, Li et al. [39] ascribed the fragmentation of nanowires to a crystalline phase transition from less stable body-centered tetragonal (BCT) to a more stable face-centered cubic (FCC) of colloidal AgNWs. They also proved that long AgNWs exhibit an inhomogeneous core-shell structure with highly strained cores and less strained sheath due to the existence of the fivefold twinning crystal structure. They claimed that the strains in the AgNWs' cores distort the common FCC crystalline lattice to BCT lattice symmetry. At elevated temperatures, the available energy for the diffusion of Ag atoms onto the surface of AgNWs becomes sufficiently high, and thus the crystalline phase transition occurs.

In order to achieve a more vivid picture of the fragmentation phenomenon, the AgNW/PS nanocomposites were suspended in CH_2Cl_2 to extract AgNWs from the nanocomposites (Figure 2). As evident in Figure 2, the fragmentation was at its early stages for our samples since most of the nanowires retained their original cylindrical geometries. However, for some nanowires the shape transformation from cylindrical to linear row of nanospheres is observable.

In order to detect the traces of silver crystalline structure, X-ray diffraction (XRD) analysis was carried out for pristine AgNWs and AgNW/PS nanocomposites. Figure 3 shows the X-ray diffractograms of AgNWs powder and AgNW/PS nanocomposites with 2.5vol% loading. Five strong characteristic peaks of silver at 2θ equal to 38.1°, 44.2°, 64.4°, 77.3° and 81.9° are clearly observable. These peaks correspond to the crystal faces of (111), (200), (220), (311) and (222) of silver face-centered cubic (FCC) crystalline structure, respectively. The X-ray diffractograms in conjunction with the TEM images confirm the successful synthesis of AgNWs and presence of AgNWs in the nanocomposites.

In the literature, Sun et al. [45] claimed that when dry AgNWs are deposited on a substrate, the orientation of all the (110) planes cannot be equally distributed due to the high aspect ratio of the nanowires. Therefore, different relative intensities of major peaks compared to standard powder diffraction pattern are expected. Furthermore, one may notice very strong (111) peak along AgNWs axial direction, which is due to the fact that the specific free energy of silver is minimum on (111) planes of the FCC structure [46]. As shown in Figure 3, no traces of crystalline silver oxide before or after processing was found by XRD. The

absence of silver oxide was also reported by other researchers who believe that silver does not form silver oxide naturally [47, 48]. Considering the conductive nature of silver and semi-conductive nature of silver oxide, the absence of silver oxide will be further verified by high conductivity and shielding of AgNW/polymer nanocomposites.

3.2. Comparison of electrical conductivity of AgNW/PS and MWCNT/PS nanocomposites

Technically, polymers are insulating and need to be filled with conductive fillers to develop lightweight electrically conductive materials. The electrical conductivity of CPCs increases nonlinearly beyond a concentration called the percolation threshold. In fact, at the percolation threshold, the first conductive path forms transforming CPCs from insulative into conductive. Physical contacts between neighboring nanofillers in combination with tunneling and hopping are the main mechanisms for the transference of electrons in CPCs [49, 50]. At filler loadings around the percolation threshold, where the conductive network is not well-established, all the aforementioned mechanisms contribute significantly to electron transference; however, at filler loadings far above the percolation threshold, the conductivity is primarily due to physical contacts between nanofillers.

Figure 4 depicts the percolation curves of the AgNW/PS and MWCNT/PS nanocomposites. The results showed that for both types of nanocomposites adding 2.5vol% conductive nanofiller into the PS matrix led to about 16 orders of magnitude enhancement in the electrical conductivity. The percolation threshold, obtained from the percolation

theory, for the MWCNT/PS nanocomposites was 0.04vol%, while the AgNW/PS nanocomposites presented a percolation threshold noticeably higher and equal to 1.2vol%.

The percolation threshold of our AgNW/PS nanocomposites is much lower than the results obtained by Sadie et al. [31] who reported percolation thresholds equal to 8.3vol%, 5.9vol% and 2.3vol% for AgNW/PS nanocomposites with the filler's aspect ratio of ~ 8, 16 and 31, respectively. This difference can be ascribed to lower diameter and larger aspect ratio of AgNWs synthesized in the current study. In another study, Sureshkumar et al. [33] synthesized AgNW with the average diameter and length of 112nm and 35µm, respectively. They coagulated AgNWs with PS, and reported a percolation threshold of 0.99vol%, which is slightly lower than ours. Lower percolation threshold reported by Sureshkumar et al. might be due to higher length of their AgNWs, however, lower diameter of AgNWs synthesized in this study is an asset for shielding applications.

Several factors could account for higher percolation threshold in the AgNW/PS nanocomposites compared to MWCNT/PS nanocomposites, namely (1) lower aspect ratio of AgNWs, (2) fragmentation phenomenon in AgNWs, and (3) inferior dispersion and distribution of AgNWs. It has been proven both theoretically and experimentally that fillers with higher aspect ratio (higher length and lower diameter) present lower percolation threshold [17]. In fact, the higher the aspect ratio of conductive fillers, the more their likelihood to neighbor or contact each other. It should be considered that the discrepancy in the aspect ratio of MWCNTs and AgNWs was intensified by the fragmentation phenomenon, where AgNWs transformed from cylindrical shapes to linear rows of nanospheres. Furthermore, inferior dispersion and distribution of AgNWs to MWCNTs

within the PS matrix, as corroborated by the TEM images, was potentially another reason for the higher percolation threshold of the AgNW/PS nanocomposites.

Figure 4 indicates that at high filler loadings, the electrical conductivity of the AgNW/PS nanocomposites is higher than the MWCNT/PS nanocomposites. For instance, at 2.5vol%, the electrical conductivity of the AgNW/PS was about twenty times higher than MWCNT/PS nanocomposites (19.2 versus $0.9 S \cdot cm^{-1}$). At filler loadings far above the percolation threshold, due to the formation of a well-established conductive network, the conductivity of CPCs relies significantly on the innate conductivity of nanofillers [38]. This justifies the higher electrical conductivity seen for the AgNW/PS nanocomposites at high filler loadings.

Figure 4 also depicts a huge difference between the maximum obtained electrical conductivity of the AgNW/PS nanocomposite and Ag bulk (19.2 versus $6.30 \times 10^{+5} S \cdot cm^{-1}$). This dissimilarity can be attributed to junction resistance and possibly the low diameter of AgNWs. Electrical measurements on individual metallic nanowires have shown that as their diameter decreases, their electrical properties deviate from bulk properties [51, 52]. This phenomenon is attributed to the presence of grain boundaries (defects) in the crystalline structure of nanowires, where electrons are scattered (either elastically or inelastically) when they try to go through a grain boundary. Nonetheless, the results of a study by Chen et al. [53] demonstrated that Ag nanobeams retain the high conductivity of bulk silver for thicknesses down to ~ 15nm. Sun et al. [29] also measured the conductivity of their in-house silver nanowire (40nm diameter) by aligning them across two gold probe electrodes, and reported conductivity values close to bulk silver conductivity. Given 25nm

as the average diameter of our synthesized AgNWs, we are uncertain whether our synthesized AgNWs suffered from the grain boundary scattering effect. This issue is beyond the scope of the current paper, and will be targeted in future studies.

3.3. EMI shielding of AgNW/PS versus MWCNT/PS nanocomposites

EMI shielding is performed by using a conductive and/or magnetic barrier to attenuate irradiated EM waves from electronics. An EM wave encompasses two components: electric field and magnetic field. The ratio of electric field to magnetic field of a propagating wave is an inherent property of a medium, and is labeled as intrinsic impedance. This ratio is considerably significant in defining the level of shielding and determining prevailing shielding mechanisms in conductive shields. The intrinsic impedance of a medium is defined as follows [23]:

$$\eta = \sqrt{\frac{j\omega\mu}{\sigma + j\omega\epsilon}} \tag{3}$$

where η is intrinsic impedance, ω is angular frequency, μ is magnetic permeability, σ is electrical conductivity and ε is real permittivity. The permittivity and permeability of free space are equal to 8.85×10^{-12}F·m^{-1} and $4\pi\times10^{-7}$H·m^{-1}, respectively. Free space has low conductivity so its intrinsic impedance is equal to 377Ω; conductive shields present significantly lower intrinsic impedance [24, 25].

Essentially, there are three mechanisms involved in the EMI shielding of CPCs, i.e. reflection, absorption and multiple-reflection. Reflection occurs due to impedance mismatch between two media. That is to say, a highly reflective shield must possess a low magnetic permeability, high electrical conductivity and/or high real permittivity. The portion of the EM wave that is not reflected infiltrates into conductive shields. As the impedance of a conductive shield is much lower than free space, a large portion of the infiltrated electric field is converted to the magnetic field. Thus, it is very important to attenuate both electric and magnetic fields inside a shield. The attenuation of the EM wave inside a conductive shield is performed through absorption mechanism, which is composed of Ohmic loss and polarization loss (electric polarization and magnetic polarization loss). The Ohmic loss is due to the interaction of propagating EM wave with nomadic charges. The Ohmic loss is in phase with the EM wave and quantified by imaginary permittivity. The polarization loss arises from the energy required to reorient electric/magnetic dipoles in each half cycle of the alternating field [22]. The levels of the electric and magnetic polarizations are represented by real permittivity and magnetic permeability, respectively.

Multiple-reflection is the third shielding mechanism in CPCs, which occurs due to the existence of huge interfacial area. Theoretically, the first reflection from the second interface of a shield is counted as a part of the reflection mechanism. According to this definition, multiple-reflection adversely impacts the overall EMI shielding due to its augmentation effect on the transmitted waves. It is believed that the multiple-reflection can be ignored if a CPC's thickness is larger than its skin depth or if shielding by absorption is more than 10dB [23]. The skin depth of a conductive shield is defined as the depth inside the

shield at which the power of the EM wave drops to 1/e of its incident value. Skin depth is proportional to the root square of electrical conductivity and magnetic permeability [25].

Figure 5 compares the average EMI shielding (overall, reflection and absorption) of the generated nanocomposites as a function of nanofiller loading over the X-band frequency range. It should be noted that the effect of multiple-reflection is included within the reported values of shielding by reflection and absorption. It was seen that the MWCNT/PS nanocomposites showed a steady ascending trend of EMI SE with increasing conductive filler loading. The overall EMI SE of the MWCNT/PS nanocomposites rose from 0.01dB for pure PS to 22.14dB for nanocomposites with 2.5vol% MWCNT loading. Surprisingly, it was observed that the AgNW/PS nanocomposites were transparent to EM waves at low AgNW loadings, and incorporating AgNW up to about 1.0vol% into the AgNW/PS nanocomposites did not enhance the EMI SE (both the reflection and absorption). However, beyond 1.0vol%, the EMI SE of the AgNW/PS nanocomposites dramatically increased. For instance, at 2.0 and 2.5vol%, the overall EMI SEs of the AgNW/PS nanocomposites were 22.70 and 31.85dB, respectively, which were significantly higher than those of their MWCNT counterparts.

The clues to understand the strange behavior of the AgNW/PS nanocomposites are in the percolation curves (Figure 4). According to the percolation curves, the percolation threshold of the MWCNT/PS and AgNW/PS nanocomposites were 0.04 and 1.20vol%, respectively, and beyond these concentrations the number of conductive networks increased. In the literature, it is believed that EMI shielding does not require filler connectivity; however it increases with filler connectivity [54]. This could justify the large

difference between the EMI shielding values of the AgNW/PS nanocomposites below and above the percolation threshold. If this is the case, Figure 5 denotes that shielding by both reflection and absorption are highly sensitive to the formation of the conductive network.

In order to validate this, we investigated the imaginary permittivity and real permittivity of the generated nanocomposites (Figure 6). It is worth mentioning that all the nanocomposites presented a non-magnetic behavior. Imaginary permittivity signifies the amount of energy dissipated by nomadic charges inside a conductive shield, and is highly sensitive to conductive network formation. It is evident that the imaginary permittivity follows the same trend as EMI SE for both types of nanocomposites. The imaginary permittivity of the AgNW/PS nanocomposites was close to zero below the percolation threshold, and then it increased pronouncedly above the percolation threshold. Drastic increase in the imaginary permittivity above the percolation threshold stems from the formation of extensive and numerous conductive networks, wherein electrons can find more mean-free-paths to go through in each half cycle of alternating field, and can dissipate more electrical energy.

Figure 6 also shows that the imaginary permittivity of the AgNW/PS nanocomposites at high loadings is much greater than MWCNT/PS nanocomposites. Several factors play a role in determining the imaginary permittivity including the innate conductivity of nanofiller, nanofillers' available surface area and the level of conductive network formation. At low filler loadings, the MWCNT/PS nanocomposites presented higher imaginary permittivity (see Figure 6) due to enhanced conductive network formation (See Figure 4) and larger available surface area (10nm diameter for MWCNTs versus 25nm

diameter for AgNWs). Nevertheless, at high filler contents, the innate conductivity of AgNW overcame its lower aspect ratio and inferior conductive network formation, leading to superior electrical properties to MWCNT/PS nanocomposites. Enhanced electrical properties of AgNWs beyond the percolation threshold commend them as futuristic materials for EMI shielding applications. Moreover, the comparison of the electrical properties of the MWCNT/PS and AgNW/PS nanocomposites confirms the dominant role of the conductive network formation on EMI shielding and imaginary permittivity.

Figure 6(b) compares the real permittivities of the generated nanocomposites, which present the same trend as the imaginary permittivity. It is seen that the real permittivity of the MWCNT/PS nanocomposites shows a uniform ascending trend with filler loading, whereas the AgNW/PS nanocomposites experienced a sudden increase in real permittivity just above the percolation threshold. In general, several polarization mechanisms can occur in CPCs depending on the structure and frequency range, i.e. interfacial, dipolar, atomic and electronic polarization [55]. However, in the current study, due to the nonpolar nature of the PS matrix and high frequency range of the X-band, the electronic polarization of the PS matrix and dipolar polarization within the nanofillers are deemed to be the only probable mechanisms in play.

Electronic polarization in CPCs originates from the concept of nanocapacitors, nanofillers act as nanoelectrodes and polymer matrix between them plays the role of nanodielectric [56, 57]. As conductive filler content approaches the percolation threshold, the thickness of nanodielectric decreases, thus the applied electric field within nanodielectric increases, leading to enhanced electronic polarization. Hence, the enhancement in the real

permittivity of the AgNW/PS nanocomposites above the percolation threshold arises from the formation of a large number of nanocapacitor structures. However, the MWCNT/PS nanocomposites experienced nanocapacitor formation at much lower loadings, i.e. 0.04vol%, and this accounts for their steady ascending trend with MWCNT content. Furthermore, the presence of defects in the crystalline structure of both MWCNT and AgNW could result in dipolar polarization and further increase of the real permittivity [58, 59].

The capacitance of a capacitor is defined as following:

$$C = \frac{\varepsilon A}{d} \quad (4)$$

where ε real permittivity, A surface area and d thickness of capacitors. Moreover, the capacitance has a direct relationship with the amount of charges stored on the surface of a capacitor. MWCNTs, due to their high aspect ratio and enhanced conductive network formation, possessed larger A and lower d than AgNWs. However, the higher innate electrical conductivity of AgNWs led to more potential charges to be stored on the surface of their nanocapacitors. Thus, there is a competition between higher surface area and enhanced conductive network of MWCNTs and superior electrical conductivity of AgNWs. The outcome of this competition was higher real permittivity (polarization loss) of the MWCNT/PS nanocomposites at low filler contents, and comparable real permittivity at high filler loadings.

4. Conclusions

AgNWs were synthesized successfully by the AC electrodeposition of Ag into porous aluminum oxide templates. AgNWs were embedded into PS via the miscible solvent mixing and precipitation technique. MWCNT/PS nanocomposites were made with the same technique for the sake of comparison. TEM and XRD analyses verified successful synthesis of AgNWs, without any traces of oxidation, with an average diameter and length of 25nm and 3.2μm, respectively. TEM images also revealed that at the molding temperature (240ºC) AgNWs transformed into a chain of nanospheres by the fragmentation phenomenon.

The percolation threshold, obtained from the percolation theory, for the MWCNT/PS nanocomposites was 0.04vol%, while the AgNW/PS nanocomposites presented a percolation threshold noticeably higher and equal to 1.2vol%. This was attributed to lower aspect ratio of AgNWs, fragmentation phenomenon in AgNWs, and inferior dispersion and distribution of AgNWs within the PS matrix.

Electrical characterization showed that at low filler loadings AgNW nanocomposites had inferior electrical properties (EMI shielding and imaginary permittivity) compared to MWCNT nanocomposites, while the electrical properties of AgNW nanocomposites surpassed their MWCNT counterparts at high filler loadings. The poorer electrical properties of AgNW/PS nanocomposites at low filler loadings were attributed to inferior conductive network and smaller filler's surface area (25nm diameter for AgNWs versus 10nm diameter for MWCNT). Nevertheless, at high filler contents, the innate conductivity

of AgNW overcame its lower aspect ratio and inferior conductive network, leading to superior electrical properties to MWCNT/PS nanocomposites. Associating the percolation curves with the electrical properties of the generated nanocomposites implied a tight correlation between EMI shielding performance and level of conductive network formation.

In conclusion, AgNWs can be introduced as futuristic conductive nanomaterials for EMI shielding applications due to their superior innate electrical conductivity and acceptable oxidation resistance.

Acknowledgements

Financial support from the Natural Sciences and Engineering Research Council of Canada (NSERC) is highly appreciated.

References

1. N. Li, Y. Huang, F. Du, X. B. He, X. Lin, H. J. Gao, Y. F. Ma, F. F. Li, Y. S. Chen and P. C. Eklund, *Nano Lett.*, 2006, 6, 1141-1145.

2. Y. K. Hong, C. Y. Lee, C. K. Jeong, J. H. Sim, K. Kim, J. Joo, M. S. Kim, J. Y. Lee, S. H. Jeong and S. W. Byun, *Curr. Appl Phys.*, 2001, 1, 439-442.

3. N. F. Colaneri and L. W. Shacklette, *IEEE Trans. Instrum. Meas.*, 1992, 41, 291-297.

4. D. Markham, *Mater. Des.*, 2000, 21, 45-50.

5. S. Y. Yang, K. Lozano, A. Lomeli, H. D. Foltz and R. Jones, *Composites Part A*, 2005, 36, 691-697.

6. J. C. Huang, *Adv. Polym. Tech.*, 1995, 14, 137-150.

7. R. W. Brown and S. M. Shvartsman, *Phys. Rev. Lett.*, 1999, 83, 1946-1949.

8. K. Takei, O. Ishii, and M. Senda, Proccedings of International Symposium on Electromagnetic Compatibility - EMC: Silicon to Systems, Symposium Record, Santa Clara, 1996, 508-510.

9. L. Su, F. Gao and L. Q. Mao, *Anal. Chem.*, 2006, 78, 2651-2657.

10. D. D. L. Chung, *Carbon*, 2001, 39, 279-285.

11. J. Joo and C. Y. Lee, *J. Appl. Phys.*, 2000, 88, 513-518.

12. J. S. Im, J. G. Kim and Y. S. Lee, *Carbon*, 2009, 47, 2640-2647.

13. J. Li, P. C. Ma, W. S. Chow, C. K. To, B. Z. Tang and J. K. Kim, *Adv. Funct. Mater.*, 2007, 17, 3207-3215.

14. A. Behnam, J. Guo and A. Ural, *J. Appl. Phys.*, 2007, 102.

15. D. Y. Kim, Y. S. Yun, H. Bak, S. Y. Cho and H. J. Jin, *Curr. Appl Phys.*, 2010, 10, 1046-1052.

16. M. Arjmand, M. Mahmoodi, S. Park and U. Sundararaj, *Compos. Sci. Technol.*, 2013, 78, 24-29.

17. Y. Huang, N. Li, Y. F. Ma, D. Feng, F. F. Li, X. B. He, X. Lin, H. J. Gao and Y. S. Chen, *Carbon*, 2007, 45, 1614-1621.

18. M. H. Al-Saleh and U. Sundararaj, *J. Phys. D: Appl. Phys.*, 2013, 46, 035304.

19. Z. Spitalsky, D. Tasis, K. Papagelis and C. Galiotis, *Prog. Polym. Sci.*, 2010, 35, 357-401.

20. W. Bauhofer and J. Z. Kovacs, *Compos. Sci. Technol.*, 2009, 69, 1486-1498.

21. E. T. Thostenson, Z. F. Ren and T. W. Chou, *Compos. Sci. Technol.*, 2001, 61, 1899-1912.

22. M. Arjmand, M. Mahmoodi, S. Park and U. Sundararaj, *J. Cell. Plast.*, 2014, 50, 551-562.

23. M. Arjmand, M. Mahmoodi, G. A. Gelves, S. Park and U. Sundararaj, *Carbon*, 2011, 49, 3430-3440.

24. P. A. Chatterton and M. A. Houlden, *NASA STI/Recon Technical Report A*, 1992, 93, 17521.

25. K. L. Kaiser, *Electromagnetic shielding*, CRC Press, Boca Raton, 2005.

26. A. Abbasi Moud, A. Javadi, H. Nazockdast, A. Fathi and V. Altstaedt, *J. Polym. Sci., Part B: Polym. Phys.*, 2014, 53, 368-378.

27. A. B. da Silva, M. Arjmand, U. Sundararaj and R. E. S. Bretas, *Polymer*, 2014, 55, 226-234.

28. R. Sachan, V. Ramos, A. Malasi, S. Yadavali, B. Bartley, H. Garcia, G. Duscher and R. Kalyanaraman, *Adv. Mater.*, 2013, 25, 2045-2050.

29. Y. Sun, Y. Yin, B. T. Mayers, T. Herricks and Y. Xia, *Chem. Mater.*, 2002, 14, 4736-4745.

30. S. Nam, H. W. Cho, S. Lim, D. Kim, H. Kim and B. J. Sung, *ACS Nano*, 2013, 7, 851-856.

31. S. I. White, R. M. Mutiso, P. M. Vora, D. Jahnke, S. Hsu, J. M. Kikkawa, J. Li, J. E. Fischer and K. I. Winey, *Adv. Funct. Mater.*, 2010, 20, 2709-2716.

32. S. I. White, P. M. Vora, J. M. Kikkawa, J. E. Fischer and K. I. Winey, *J. Phys. Chem C*, 2010, 114, 22106-22112.

33. M. Sureshkumar, H. Y. Na, K. H. Ahn and S. J. Lee, *ACS Appl. Mater. Interfaces*, 2015, 7, 756-764.

34. J. Ma, M. Zhan and K. Wang, *ACS Appl. Mater. Interfaces*, 2015, 7, 563-576.

35. Y.-H. Yu, C.-C. M. Ma, C.-C. Teng, Y.-L. Huang, S.-H. Lee, I. Wang and M.-H. Wei, *Mater. Chem. Phys.*, 2012, 136, 334-340.

36. M. Hu, J. Gao, Y. Dong, K. Li, G. Shan, S. Yang and R. K.-Y. Li, *Langmuir*, 2012, 28, 7101-7106.

37. G. A. Gelves, M. H. Al-Saleh and U. Sundararaj, *J. Mater. Chem.*, 2011, 21, 829-836.

38. G. A. Gelves, B. Lin, U. Sundararaj and J. A. Haber, *Adv. Funct. Mater.*, 2006, 16, 2423-2430.

39. Z. Li, J. S. Okasinski, J. D. Almer, Y. Ren, X. Zuo and Y. Sun, *Nanoscale*, 2014, 6, 365-370.

40. M. E. Toimil-Molares, A. G. Balogh, T. W. Cornelius, R. Neumann and C. Trautmann, *Appl. Phys. Lett.*, 2004, 85, 5337-5339.

41. S. Karim, M. E. Toimil-Molares, A. G. Balogh, W. Ensinger, T. W. Cornelius, E. U. Khan and R. Neumann, *Nanotechnology*, 2006, 17, 5954-5959.

42. K. F. Gurski and G. B. McFadden, *Proc. R. Soc. Lond. A*, 2003, 459, 2575-2598.

43. K. F. Gurski, G. B. McFadden and M. J. Miksis, *SIAM J. Appl. Math.*, 2006, 66, 1163-1187.

44. T. Muller, K. H. Heinig and B. Schmidt, *Mater. Sci. Eng., C*, 2002, 19, 209-213.

45. Y. Sun, Y. Ren, Y. Liu, J. Wen, J. S. Okasinski and D. J. Miller, *Nat. Commun.*, 2012, 3, 971.

46. S. Liu, R. J. Wehmschulte, G. Lian and C. M. Burba, *J. Solid State Chem.*, 2006, 179, 696-701.

47. W. Campbell and U. Thomas, *Trnas. Electrochem. Soc.*, 1939, 76, 303-328.

48. A. Czanderna, *J. Phys. Chem.*, 1964, 68, 2765-2771.

49. I. Balberg, *Phys. Rev. Lett.*, 1987, 59, 1305-1308.

50. E. K. Sichel, J. I. Gittleman and P. Sheng, *Phys. Rev. B*, 1978, 18, 5712-5716.

51. W. Steinhogl, G. Schindler, G. Steinlesberger and M. Engelhardt, *Phys. Rev. B*, 2002, 66, 075414 (1-4).

52. W. Wu, S. H. Brongersma, M. Van Hove and K. Maex, *Appl. Phys. Lett.*, 2004, 84, 2838-2840.

53. J. Y. Chen, B. J. Wiley and Y. N. Xia, *Langmuir*, 2007, 23, 4120-4129.

54. M. Arjmand, T. Apperley, M. Okoniewski and U. Sundararaj, *Carbon*, 2012, 50, 5126-5134.

55. M. Arjmand, Ph.D. Thesis , University of Calgary, 2014.

56. Y. Shen, Y. Lin, M. Li and C. W. Nan, *Adv. Mater.*, 2007, 19, 1418-1422.

57. P. M. Raj, D. Balaraman, V. Govind, L. Wan, R. Abothu, R. Gerhardt, S. Bhattacharya, M. Swaminathan and R. Tummala, *IEEE Trans. Compon. Packag. Manuf. Technol.*, 2007, 30, 569-578.

58. J.-K. Yuan, S.-H. Yao, Z.-M. Dang, A. Sylvestre, M. Genestoux and J. Bai1, *J. Phys. Chem. C*, 2011, 115, 5515-5521.

59. M.-J. Jiang, Z.-M. Dang, M. Bozlar, F. Miomandre and J. Bai, *J. Appl. Phys.*, 2009, 106, 084902.

Figure Captions:

Figure 1: (a) TEM micrographs of (a) pristine AgNWs, (b) 1.5vol% AgNW/PS nanocomposite, and (c) 1.5vol% MWCNT/PS nanocomposite.

Figure 2: Fragmentation in AgNW/PS nanocomposites at two various magnifications. AgNWs were extracted from 2.5vol% AgNW/PS nanocomposites employing CH_2Cl_2; (a) low magnification (b) high magnification.

Figure 3: XRD pattern of (a) AgNWs powder right after liberation, (b) AgNW/PS nanocomposite having 2.5vol% AgNWs.

Figure 4: Electrical conductivity of AgNW/PS versus MWCNT/PS nanocomposites as a function of nanofiller loading.

Figure 5: EMI SE (overall, reflection and absorption) of AgNW/PS and MWCNT/PS nanocomposites as a function of nanofiller loading.

Figure 6: (a) Imaginary permittivity, and (b) real permittivity as a function of nanofiller loading.

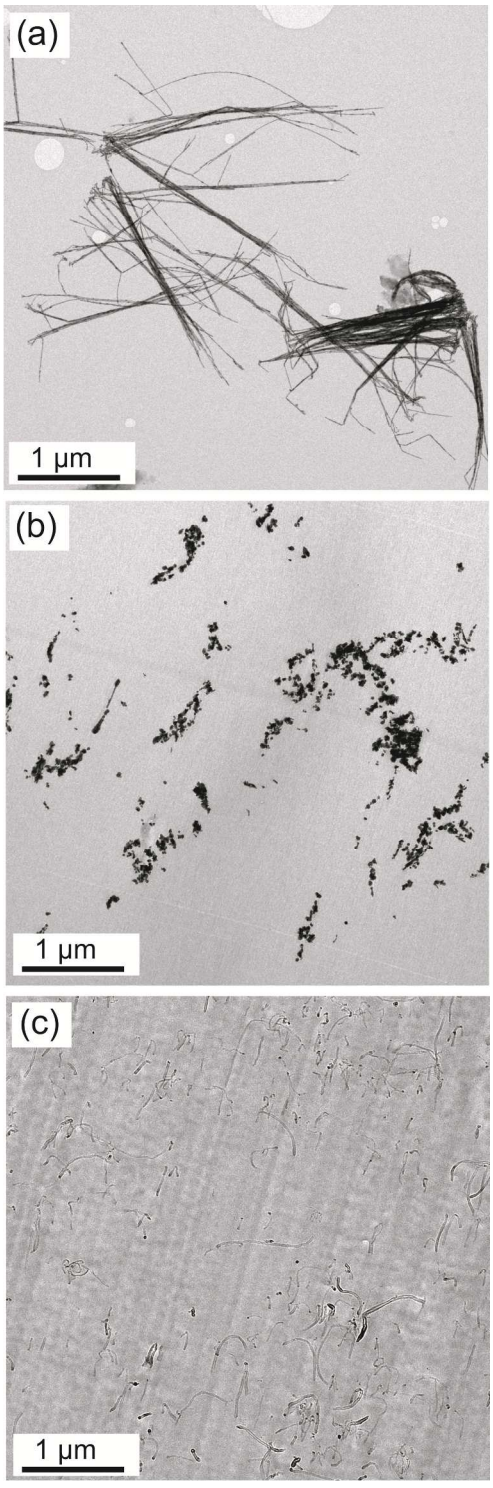

Figure 1: (a) TEM micrographs of (a) pristine AgNWs, (b) 1.5vol% AgNW/PS nanocomposite, and (c) 1.5vol% MWCNT/PS nanocomposite.

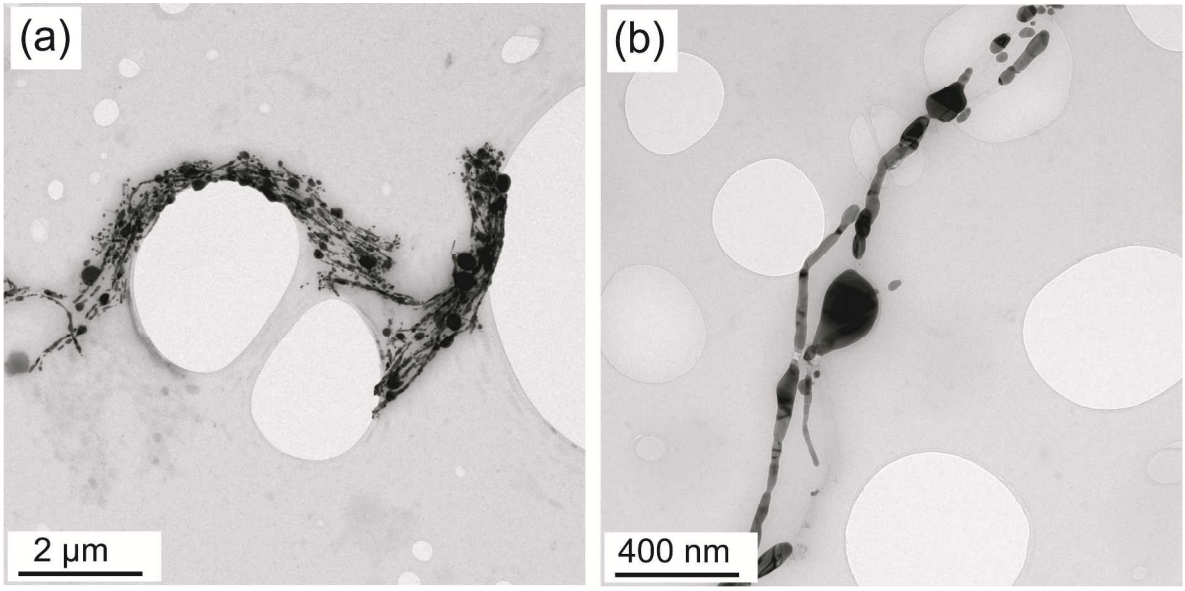

Figure 2: Fragmentation in AgNW/PS nanocomposites at two various magnifications. AgNWs were extracted from 2.5vol% AgNW/PS nanocomposites employing CH_2Cl_2; (a) low magnification (b) high magnification.

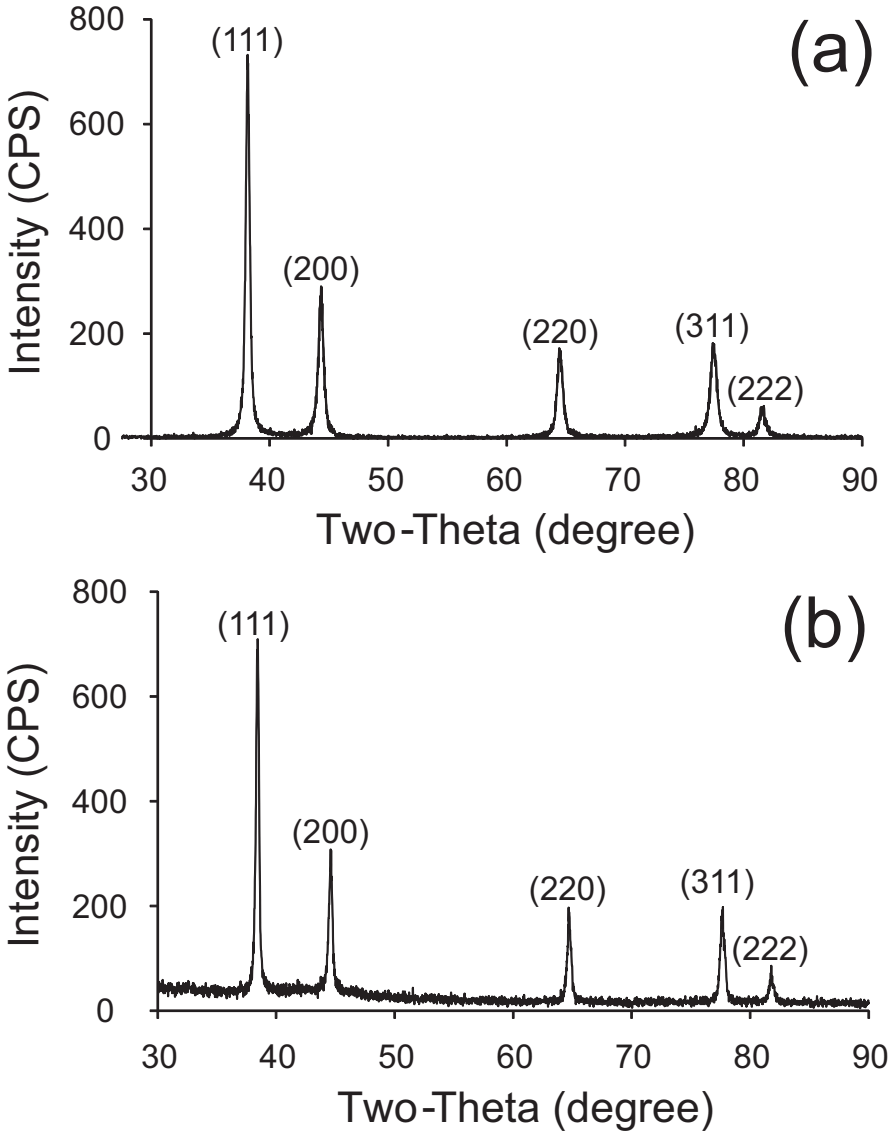

Figure 3: XRD pattern of (a) AgNWs powder right after liberation, (b) AgNW/PS nanocomposite having 2.5vol% AgNWs.

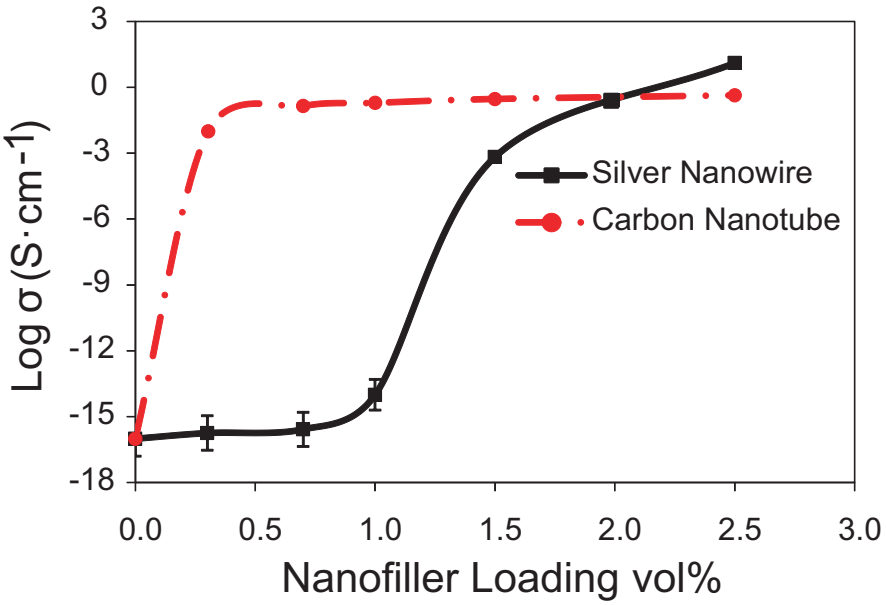

Figure 4: Electrical conductivity of AgNW/PS versus MWCNT/PS nanocomposites as a function of nanofiller loading.

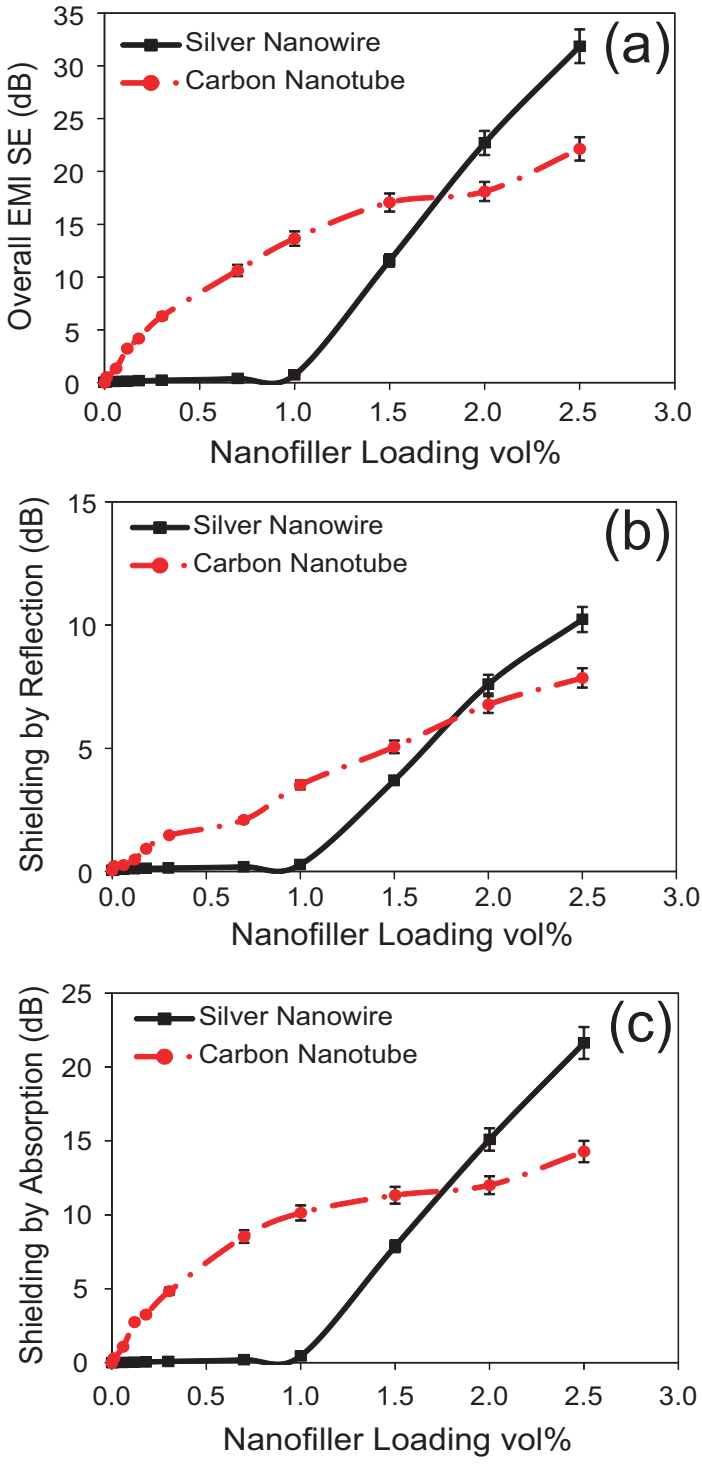

Figure 5: EMI SE (overall, reflection and absorption) of AgNW/PS and MWCNT/PS nanocomposites as a function of nanofiller loading.

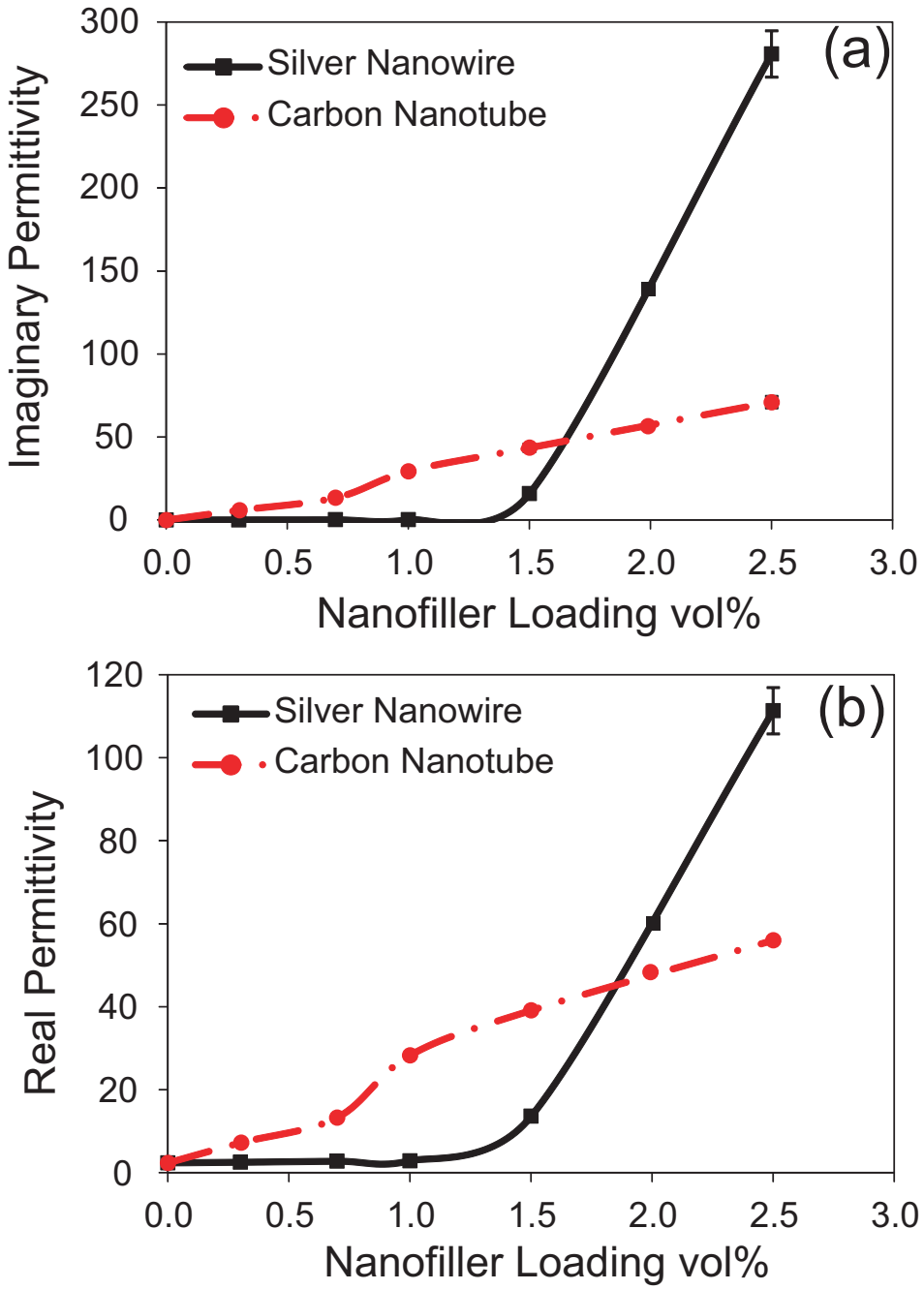

Figure 6: (a) Imaginary permittivity, and (b) real permittivity as a function of nanofiller loading.